

Article

Changes in Atmospheric, Meteorological, and Ocean Parameters Associated with the 12 January 2020 Taal Volcanic Eruption

Feng Jing ¹, Akshansha Chauhan ², Ramesh P Singh ^{3,*} and Prasanjit Dash ⁴

¹ Institute of Earthquake Forecasting, China Earthquake Administration, Beijing 100036, China; jingfeng@cea-ies.ac.cn

² Department of Environmental Sciences, Sharda University, Greater Noida 201310, India; akshansha1886@gmail.com

³ School of Life and Environmental Sciences, Schmid College of Science and Technology, Chapman University, Orange, CA 92866, USA

⁴ NOAA Center for Satellite Applications & Research, Cooperative Institute for Research in Atmosphere (CIRA), Colorado State University, College Park, MD 20740, USA; Prasanjit.Dash@noaa.gov

* Correspondence: rsingh@chapman.edu

Received: 27 February 2020; Accepted: 20 March 2020; Published: 23 March 2020



Abstract: The Taal volcano erupted on 12 January 2020, the first time since 1977. About 35 mild earthquakes (magnitude greater than 4.0) were observed on 12 January 2020 induced from the eruption. In the present paper, we analyzed optical properties of volcanic aerosols, volcanic gas emission, ocean parameters using multi-satellite sensors, namely, MODIS (Moderate Resolution Imaging Spectroradiometer), AIRS (Atmospheric Infrared Sounder), OMI (Ozone Monitoring Instrument), TROPOMI (TROPOspheric Monitoring Instrument) and ground observations, namely, Argo, and AERONET (AEROSOL ROBOTIC NETWORK) data. Our detailed analysis shows pronounced changes in all the parameters, which mainly occurred in the western and south-western regions because the airmass of the Taal volcano spreads westward according to the analysis of airmass trajectories and wind directions. The presence of finer particles has been observed by analyzing aerosol properties that can be attributed to the volcanic plume after the eruption. We have also observed an enhancement in SO₂, CO, and water vapor, and a decrease in Ozone after a few days of the eruption. The unusual variations in salinity, sea temperature, and surface latent heat flux have been observed as a result of the ash from the Taal volcano in the south-west and south-east over the ocean. Our results demonstrate that the observations combining satellite with ground data could provide important information about the changes in the atmosphere, meteorology, and ocean parameters associated with the Taal volcanic eruption.

Keywords: Taal volcano; satellite remote sensing; AOD; gas emission; Argo; ocean parameters

1. Introduction

Active volcanoes exist throughout the world and are distributed in different continents. In the past, more than 1500 volcanoes have erupted [1]. Volcanic eruptions are one of the deadly natural disasters that may cause extensive damage by thick hot ashes and lava flows. The associated emissions have long term impacts on agriculture, glaciers, aviation, ecology, environment, air quality, human health, solar activity, atmosphere, and ocean water when a volcano is located near the ocean coast [2–11]. The impact of a volcanic ash plume has been observed in the Asian summer monsoon associated with the Sarychev eruption in 2009 [12]. During a volcanic eruption, several gases are emitted, and generally, the amount of sulfur dioxide (SO₂) is very high. The gases from the volcano are dispersed

in directions depending on the prevailing wind directions, and the extent depends on the moisture content of the ash and wind velocity. The extent of SO₂ from the source of eruption can even reach up to 2700 km [13]. A large amount of gases and particulate matters were injected in the atmosphere due to volcanic eruption, dispersed in all the directions affecting the air quality and visibility. The suspended particulate matters remain in the surrounding volcanic areas. The heavier wet ashes may settle early and get dispersed later. In the past, due to volcanic ash impacts, flights were interrupted for many days as the particulates can impact the airplane engine causing serious disaster [4,7,14,15]. During and even before the volcanic eruptions, pronounced changes in surface and subsurface stress have occurred that may have triggered volcanic earthquakes. Due to SO₂ emissions from volcanic eruptions, a general cooling of globally averaged surface temperatures for a few years after the eruption due to a barrier effect to sunlight caused by ash and aerosol-cloud has been observed, as was evident by the 1991 Mt Pinatubo eruption [16,17].

Ground observation is a conventional way to monitor volcanic activities due to its high accuracy, but it is difficult to obtain continuous data of the required spatial coverage. Almost half of the subaerial volcanoes in the globe have no ground monitoring system [18]. Compared to ground observations, satellite observations provide various information related to volcanic activities, including surface deformation, SO₂ emission, heat flux, volcanic ash retrieval, crater lake temperature, and water chemistry [19–21], although it has a relatively lower spatial resolution. The lava flow cooling and topographic changes in the sub-flow have been observed using Landsat TM infrared data [22]. Pergola et al. [23] proposed the Robust AVHRR Techniques (RAT) approach to detect volcanic hotspots. The method, renamed as Robust Satellite Techniques (RST), was used to monitor thermal volcanic activity and track volcanic plumes by means of polar and geostationary satellite data [24–26]. TanDEM-X (TerraSAR-X add-on for Digital Elevation Measurement) data provides an ability to obtain a four-dimensional evolution of volcanic lava flow [27]. Also, high spatial resolution multispectral satellite data provide an important complement for field observations for monitoring active lava flows [28] and risk assessment of lava flows [29].

Satellite observations provide evidence for the impact of volcanic eruption on the marine ecological environment. Duggen et al. [30] found that the deposition of volcanic ash on the ocean surface could fertilize ocean water and enhance diatom growth. They observed different ocean color and enhanced chlorophyll concentration using Moderate Resolution Imaging Spectroradiometer (MODIS) data. Recently, an increase in chlorophyll concentrations was observed on the subarctic North Pacific about one to two weeks after the volcanic eruption in the Aleutian Islands using MODIS chlorophyll data, which could be associated with the iron fertilization from the volcano that enhances ocean productivity [31,32].

Volcanic degassing is an important part of volcano monitoring. SO₂ emission is one of the indicators used to monitor volcanic activities and forecast eruptions [33], and it is the most common volcanic gas observed from space due to the low background concentration compared to other volcanic gases, such as H₂O and CO₂ [34]. The GOME (the Global Ozone Monitoring Experiment) instrument onboard ERS-2 (European Remote Sensing Satellite-2) provided enhanced SO₂ information during the period of volcanic eruption and degassing [35], despite the low spatial resolution (40 × 320 km). Recently, SO₂ emission data with high spatial, temporal, and spectral resolutions observed by satellites has been used for SO₂ flux assessment [36], SO₂ plume mapping [37], and also weak SO₂ emission detection [38]. Besides SO₂, satellite observation also provides evidence of the release of other volcanic gases, such as carbon monoxide [39], hydrogen chloride [40], and hydrogen sulfide [41].

Multi-sensor satellite data have also been used to evaluate the consistency of the characteristics of volcanic emissions [21,42] and SO₂ mass loadings [43]. Considering the advantages and disadvantages of ground-based and satellite-based observations, two kinds of data have been integrated to obtain thermal behavior [44], lava flows [45], SO₂ emission [20,46,47], and volcanic plume evolution [48,49].

The Taal volcano is surrounded by a lake and ocean. Detailed analysis of ground, satellite, Argo floats, and AERONET (AERosol RObotic NETwork) data have been carried out to study the impacts of

the Taal volcanic eruption on ocean, atmosphere, and meteorological parameters. The results discussed in the present paper clearly show pronounced changes in all the parameters.

2. Taal Volcano

2.1. The eruption of 12 January 2020

On 12 January 2020 at 2.30 p.m. (local time), an explosive eruption produced a giant plume of volcanic ash up to 15 km in the atmosphere and extending up to about 67 km south of the capital city of Manila [50] and beyond, up to the city of Quezon about 70 km away from the location of the Taal volcano. Over 50,000 people were affected, and Manila International airport suspended all flights. The Taal island and surrounding provinces were evacuated [50]. Within 24 h of the eruption, about 450 earthquakes were felt with the emergence of fissures and receding of the surrounding lake. The observed seismic activities suggest a rise of magma from deep in the earth [50].

The Taal volcano is an active volcano located on the southwest of the Luzon island in the Philippines. Figure 1 shows the geolocation of Taal Volcano and its surroundings, with ocean water close to the volcano. Taal Volcano is surrounded by the Taal lake outside and the main crater lake inside. Historically, over a 10°C increase in temperature of the crater lake has been observed before the eruption in September 1965 [51].

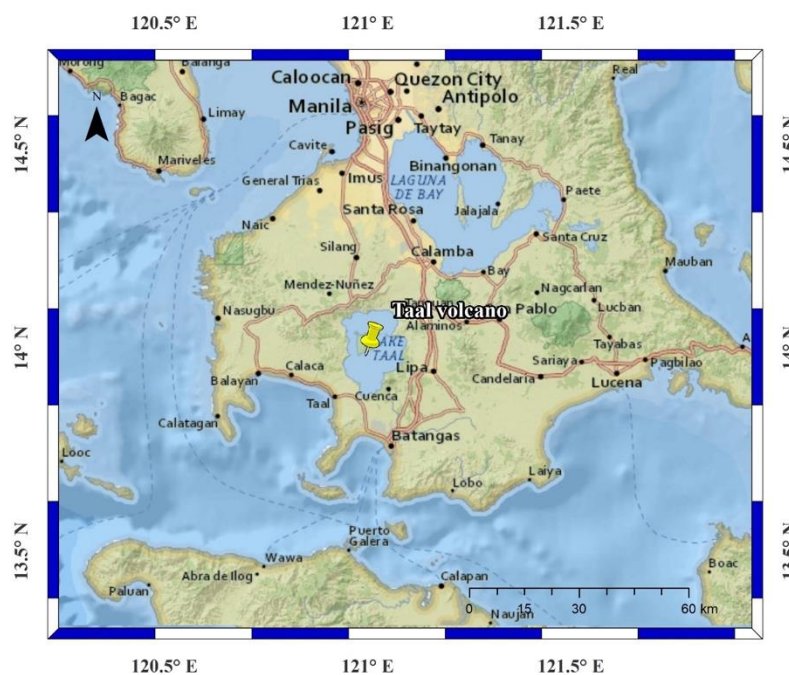


Figure 1. Geographical location and surrounding environment of the Taal volcano (Source of the base map: National Geographic).

Taal Volcano was classified as “DECADE VOLCANOES” by the International Association of Volcanology and Chemistry of the Earth’s Interior (IAVCEI). A total of 33 historical eruptions have been recorded, excluding the newest one [52], but the latest study has shown that only 24 of the 33 historic events are confirmed, and the other nine should be considered for reassessment [53]. The last eruption of the Taal volcano occurred on 3–4 October 1977, and afterward, it remained quiet, but more than 20 earthquake swarms were recorded until 12 January 2020 [53]. No other signals were observed about an impending volcanic eruption, which occurred on 12 January 2020. Details of the volcano and associated links are available from the US National Museum of Natural History’s Global Volcanism Program (<https://volcano.si.edu/volcano.cfm?vn=273070>).

2.2. Volcano monitoring

Earlier, in December 1952, monitoring of Taal Volcano started, and the first volcanological station was established by the Commission on Volcanology (COMVOL) in Brgy. The station was equipped with a three-components low sensitivity seismograph: a water-tube tiltmeter, thermometers, and short-wave radio transmitters. On 28 September 1965, all the instruments were destroyed due to the onset of a phreatomagmatic phase of the Mt. Tabaro eruption. In 1966, a new Pira-piraso station was established on the northern shore of Volcano Island with seismographs and a tiltmeter, these instruments were updated in 1968 and again in 1970. At the northern shore of Taal Lake, Buco observatory was constructed from 1969 to 1970, which was handed over to COMVOL after completion with a similar set of instruments and a speed boat. The observatory was reconstructed in 2016 after severe damage from a blown-down century-old acacia tree during the passage of Typhoon Glenda in 2015 (<https://www.phivolcs.dost.gov.ph/index.php/volcano-hazard/volcano-monitoring2/volcano-observatory>).

During the last 40 years, no eruptive activity was recorded; given the past eruption history, an unusual quiescence period was realized by the scientists. Seismological [54,55], geochemical [56], electromagnetic [55,57], thermal [52,58], and InSAR crustal deformation measurement [59] techniques were used to monitor activities of the Taal volcano. Efforts were made to map the 3-D structure and monitor the volcanic activities and observations of geophysical parameters (magnetic, electric, tilt, resistivity, ground and water temperature). All these geophysical parameters were recorded at the field sites and telemetered to PHIVOLCS (The Philippine Institute of Volcanology and Seismology). A shallow magmatic source located at a depth 4–6 km below the current Main Crater Lake on Volcano Island were delineated [52,55,57].

Due to the long gap in eruption period, it was expected that the next eruption would be large (volcanic explosive index—VEI ≥ 4) and more likely that the eruption would occur from another cone surrounding the main crater (PHIVOLCS <http://www.phivolcs.dost.gov.ph/>). Through an international cooperative program involving teams from Japan, France, USA, Greece, Italy, and Belgium, training to PHIVOLCS members about the installation techniques, analysis of electromagnetic data, and ways to monitor the volcano were given.

2.3. Earthquake activities around Taal Volcano

The Taal volcano area is seismically active. Figure 2a shows the frequency of mild earthquakes within a radius of 150 km around the Taal volcano, downloaded from the USGS (United States Geological Survey) website (<https://earthquake.usgs.gov/earthquakes>) during the period 25 January 2000 to 10 February 2020. The two largest earthquakes occurred on 8 October 2004 with a magnitude of 6.5 and a focal depth of 105 km, and another earthquake on 11 August 2017 with a magnitude of 6.2 and a focal depth of 172 km. Both these earthquakes were located within 50 km around the Taal volcano (PHIVOLCS <http://www.phivolcs.dost.gov.ph/>).

Figure 2b shows the spatial distribution of the earthquake epicenters with a magnitude greater than 4.0 mb within a 50 km radius around the Taal volcano during the period 1 November 2019 – 9 March 2020. On the day of the Taal eruption, a total number of 35 earthquakes (magnitude with 4.2–4.7 mb) occurred and continued for 24 h. Figure 2c shows the temporal distribution of earthquake activities (magnitude greater than 4.0 mb) within a 50 km radius around the Taal volcano between 1 November 2019 and 9 March 2020 from the USGS website. Prior to 12 January 2020, four earthquakes (magnitude 4.8, 4.0, 4.4, and 4.1 mb) occurred, respectively, on 15 November 2019, and 2, 9, and 24 December 2019. It is difficult for us to access a detailed catalog of earthquakes, so we cannot comment on the frequency of small earthquakes.

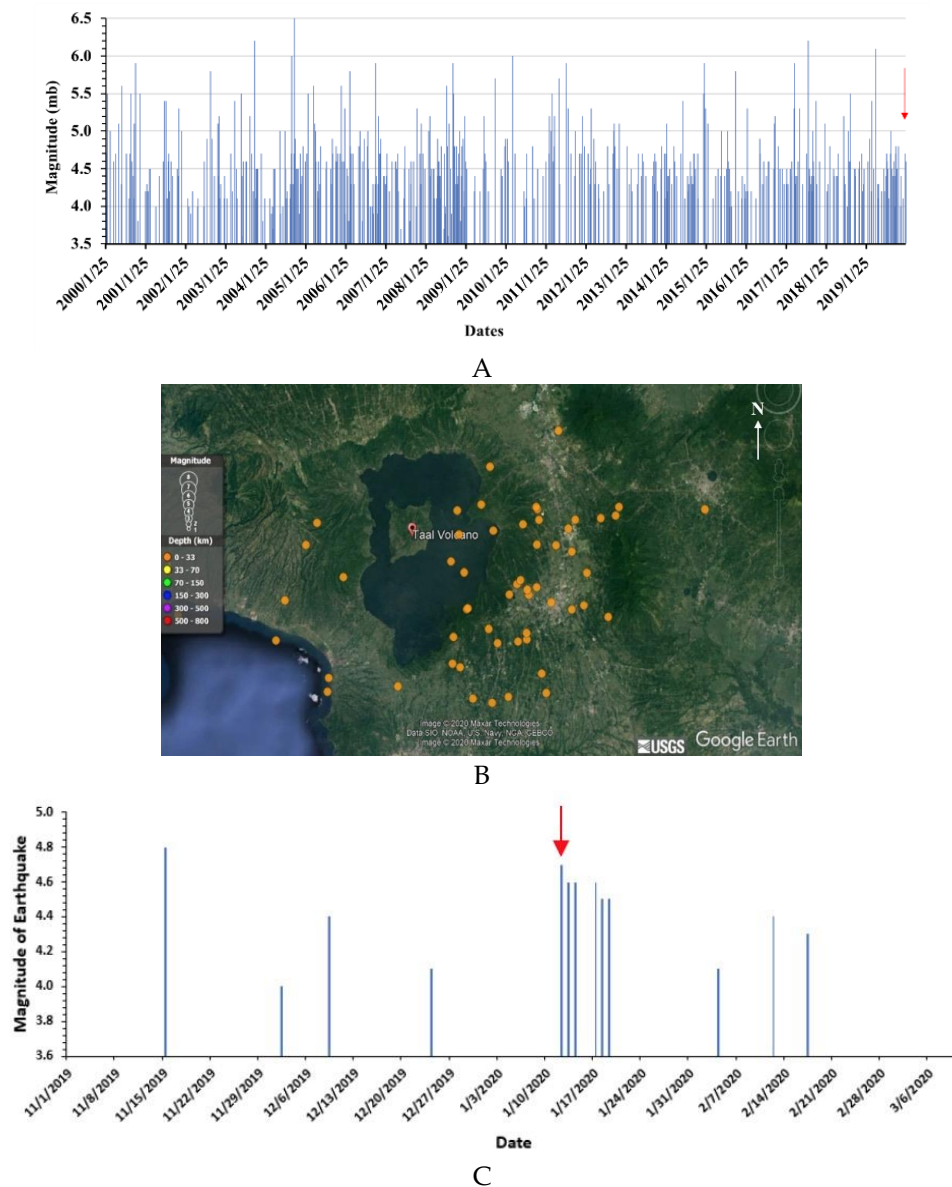


Figure 2. (a) Distribution of earthquakes within a 150 km radius around the Taal Volcano from 25 January 2000 – 10 February 2020. The volcanic eruptions started on 12 January 2020, as indicated by the red arrow. (b) Distribution of earthquakes with magnitude greater than 4.0 mb (yellow dots) within a 50 km radius around the Taal volcano from 1 November 2019 to 9 March 2020. Yellow dots show the distribution of earthquake epicenters. A total of 35 earthquakes occurred on 12 January 2020, and afterward, 18 earthquakes occurred on 13 January 2020. (c) Distribution of earthquake magnitudes greater than 4.0 mb within a radius of 50 km from 1 November 2019 to 9 March 2020 around the Taal Volcano, data are taken from the USGS website. Soon after the volcanic eruption (red arrow), the frequency of mild magnitude earthquakes increased. We do not have access to the local earthquake catalog, so we cannot comment on small earthquakes; however, a few earthquakes of magnitude around 4.0 and larger have been observed (source: USGS).

3. Data and methods

3.1. Satellite data

The satellite data considered in the detailed analysis are given in Table 1. We used the MODIS aerosol optical depth (AOD) products (collection 6.1) [60] from the MODIS sensor through the NASA Giovanni portal (<https://giovanni.gsfc.nasa.gov/giovanni/>). For better temporal coverage, we have

taken the mean of Terra and Aqua MODIS data for an individual day. Total Column Ozone (TCO) data observed by AIRS (Atmospheric Infrared Sounder) [61], onboard the Earth Observing System (EOS) polar-orbiting platform, was also used in the present work. We have considered an average of ascending (daytime) and descending (nighttime) modes data; ascending mode is when the satellite passes from south to north, whereas the descending mode is when the satellite passes from north to south over the Earth's surface. In ascending mode, the local pass time is around 1.30 p.m. (daytime), and in descending mode, local pass time is around 1.30 a.m. (nighttime) for the AIRS satellite. The AIRS daily L3 retrieved products—water vapor and relative humidity products—have been considered in the present work. These products have global coverage at a spatial resolution of $1.0 \times 1.0^\circ$ [62]. Volcanoes are known to emit SO_2 in the atmosphere. We have considered the Column Amount of SO_2 (Planetary Boundary Layer) acquired by an Ozone Monitoring Instrument (OMI) [63], which measures the atmospheric aerosols properties and also differentiates between smoke aerosols, dust, and sulfates. OMI is one of the four instruments of the NASA Aura satellite mission, which passes the equator at 01:45 p.m. It observes the backscattered sunlight by various molecules in visible and UV bands with the help of a wide-field telescope. These telescopes relate to two imaging grating spectrometers, which help in the measurement of Ozone, NO_2 , SO_2 , and atmospheric aerosols. These satellite data are also downloaded through the NASA Giovanni portal.

Table 1. Details of satellite data used in this paper.

Data	Satellite	Instrument	Spatial Resolution
AOD	Terra/Aqua	MODIS	$1.0 \times 1.0^\circ$
SO_2	Aura	OMI	$0.25 \times 0.25^\circ$
	Sentinel-5P	TROPOMI	$5.5 \times 3.5 \text{ km}$
Ozone	Terra/Aqua	AIRS	$1.0 \times 1.0^\circ$
	Sentinel-5P	TROPOMI	$5.5 \times 3.5 \text{ km}$
CO	Terra/Aqua	AIRS	$1.0 \times 1.0^\circ$
	Sentinel-5P	TROPOMI	$5.5 \times 7 \text{ km}$
Water vapor/Relative humidity	Terra/Aqua	AIRS	$1.0 \times 1.0^\circ$

Sentinel-5P TROPOMI (TROPOspheric Monitoring Instrument) SO_2 , Ozone, and carbon monoxide (CO) datasets with high spatial, temporal, and spectral resolutions have been used in this study. The Sentinel-5P satellite was launched on 13 October 2017. The spatial resolution of TROPOMI SO_2 and Ozone data is $5.5 \times 3.5 \text{ km}$. The available SO_2 and Ozone datasets were generated by the DOAS (Differential Optical Absorption Spectroscopy) method [64] and the direct-fitting algorithm [65], respectively. The TROPOMI CO dataset, with a spatial resolution of $5.5 \times 7 \text{ km}$ was retrieved with the SICOR (Shortwave Infrared Carbon Monoxide Retrieval) algorithm [66].

3.2. Ground observation data

We have used the Manila AERONET station (14.63° N , 121.07° E) data (67 km areal distance from the Taal volcano) (Figure 3). The AERONET is a ground-based network that uses sun and sky radiometers located throughout the world [67]. These stations help in the study of aerosols properties at local, regional, and global scales. The methodology of retrieval of aerosol parameters (aerosol optical depth—AOD, angstrom exponent—AE, the radius of the particles, and single scattering albedo—SSA, etc.) from AERONET stations has been discussed in detail by Dubovik and King [68] and Dubovik et al. [69]. In the present study, we have used AOD, AE, SSA, and the particle size distribution of aerosols coming from the source, Taal volcano. The data used is version 3 and level 1.5 data, as the quality-controlled level 2.0 data were not available at the time of analysis. These parameters are available through the web (<https://aeronet.gsfc.nasa.gov/>).

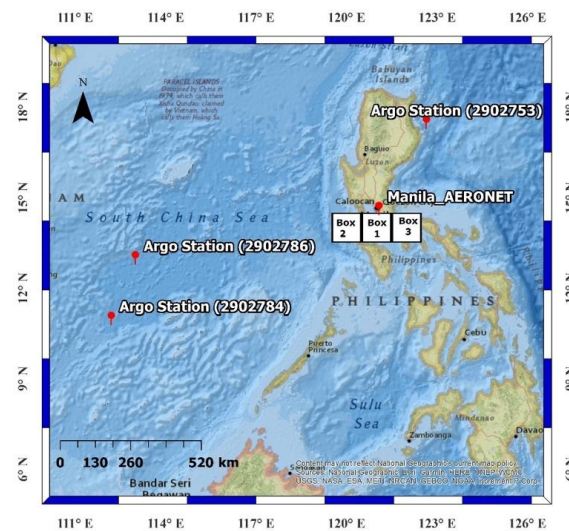


Figure 3. Locations of various Argo stations and the Manila AERONET station along with three boxes chosen for the analysis of various parameters using satellite data. (Bathymetry base map source: National Geographic).

The Argo Program is part of the Global Ocean Observing System. Argo floats are deployed in the oceans throughout the world. Argo floats data are used in this work to study the temporal changes in water temperature and salinity. Argo data are collected and made freely available by the International Argo Program, and different countries also run their Argo stations and contribute to the international efforts (www.argo.ucsd.edu; argo.jcommops.org). Data and automatic quality checks are discussed in detail by Wong et al. [70]. The vertical resolution is different for different parameters, and the data sets are available with time intervals of 5 days [71]. We used data from three Bio-Argo floats (see Figure 3 for their locations): station [2902786] is in the direct path of the plume (according to the forward trajectory model shown in Figure 4), and station [2902784] is close to the region that is directly affected by volcanic emission. The station [2902753] is not located in the direct path of the plume coming from the Taal volcano. The data coming from the three stations are taken to analyze the vertical profile of the ocean variables from ~5 to 1000 m.

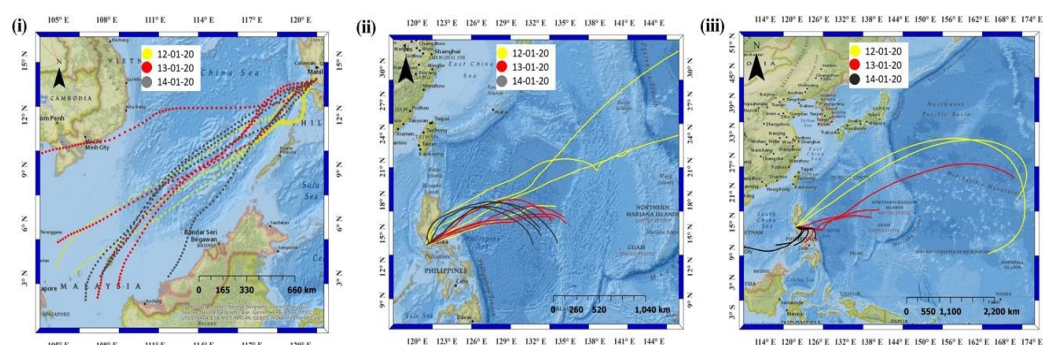


Figure 4. National Oceanic and Atmospheric Administration (NOAA) Hybrid Single Particle Lagrangian Integrated Trajectory (HYSPLIT) forward trajectory at (i) 500, (ii) 5000, and (iii) 10,000 m heights, sourced from the Taal volcano for 150 h run time between 12 and 14 January 2020. The influence of the ash plume is seen over the south-west and north-eastern region from the Taal volcano from different heights and parts of Cambodia and Malaysia. (Source of the base map: National Geographic).

3.3. Modeling data

The NOAA air trajectory model—the Hybrid Single Particle Lagrangian Integrated Trajectory Model Version 4 (HYSPLIT4) for forward trajectories—was used to study the transport of ash coming

from the Taal eruption. We carried out the HYSPLIT forward trajectories calculation for a 150 h run and with a time interval of 6 h at 500, 5000, and 10,000 m heights, the trajectories show the transport of air mass from the Taal volcano eruptions during 12 – 14 January 2020 (Figure 4).

Air mass transport from a height of 500 m from the Taal volcano is seen over the ocean and coastal parts of Cambodia and Malaysia (Figure 4i). The transport of air mass from the higher altitude affected the north-eastern oceanic regions of the Philippines, and on 14 January 2020, the air mass affected the southern Philippines from a 10 km altitude (Figure 4ii,iii). The wind direction at the height of 500 m was in the north-east direction, which brings volcanic ash towards the north-west direction, whereas at 5000 and 10,000 m, the wind direction was in the south to south-westerly and dispersed volcanic ash in the north-east direction, which is clearly reflected from the forward trajectories (Figure 4). During the Taal volcanic eruptions, ash was injected into the atmosphere up to a height of 14.5 km (https://so2.gsfc.nasa.gov/omps_2012_now.html#2020). The wind directions at different altitudes were observed from vector wind analysis using NOAA NCAR Reanalysis-II over the Philippines and close to the ground at a pressure level of 1000hPa. Near the surface, the wind was north-easterly, and at 600 hPa and 250 hPa pressure levels, the wind was westerly and south-westerly, which dispersed volcanic ash to the north-east to the Taal volcano (Figure 4ii,iii).

The National Climatic Data Center (NCDC) of the US National Oceanic and Atmospheric Administration (NOAA) (www.ncdc.noaa.gov) provides access to various meteorological parameters for Manila station. These parameters are calculated by using modeling, assimilation techniques, and ground observations. The wind data has a 3-h temporal resolution for each day.

The wind rose diagrams at Kota Kinabalu, Sabah, Malaysia, and San Juan, Batangas, Philippines, were plotted using Weather Underground data (www.wunderground.com/history) (Figure 5). The website provides real-time and historical data at various airports around the world. The wind data at Sabah, Malaysia, has half-hour temporal resolution, and at Batangas, Philippines, temporal resolution is one hour. The Manila wind rose diagram shown in Figure 5 is based on the wind data taken from NOAA NCDC.

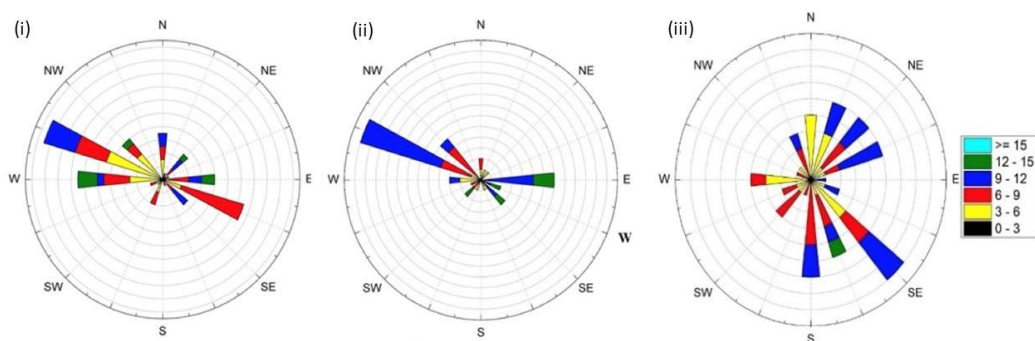


Figure 5. Rose diagrams of wind over (i) Sabah, Malaysia, (ii) Batangas, Philippines, from 12-14 January 2020 and (iii) Manila, Philippines, from 12-17 January 2020 showing dominant wind south-east and north-east directions. The emissions from the Taal volcano may be dispersed in all the directions in the proximity of the Taal volcano since the wind shows all the directions, with the dominant wind in the south-east.

4. Results

We have considered three areas ($1 \times 1^\circ$), Box 1 over Taal, Box 2 on the west side, and Box 3 on the east side (Figure 3) to carry out a detailed analysis of satellite data for atmospheric and meteorological parameters for the period 31 December 2019 – 31 January 2020. Spatial variations of SO_2 , Ozone, CO, sea surface temperature, and surface latent heat flux around the time of the Taal eruption have been analyzed.

4.1. Properties of volcanic aerosols

Figure 6a shows the mean of Terra and Aqua MODIS AOD for better temporal resolution over three boxes for the periods 31 December – 31 January 2020. The mean AOD for January 2020 is found to be 0.17, 0.12, and 0.18 for Boxes 1, 2, and 3, respectively. A sharp increase in the AOD value just after the volcanic eruption is observed over Boxes 1 and 2 as the shift of the airmass is seen towards the western and south-western regions as appeared from the forward trajectory of airmass from the Taal volcano (Figure 4i–iii) and wind directions (Figure 5). We have also analyzed the aerosol properties (AOD, AE, and Total Column Water—TCW) at the AERONET station in Manila using AERONET data (Figure 6b). The averaged AOD, AE, and TCW values during January 2020, respectively, are found to be 0.24, 1.2, and 3.42 cm. The small component of the western and south-west winds impacted the optical properties at Manila, and about 10.74% and 12.15% enhancement in AE are observed on 14 and 15 January 2020 (Figure 6b). No data are available for 12 and 13 January 2020 due to volcanic ash in the atmosphere that affected the visibility of a large region. Changes in AE with lower AOD values (0.22 and 0.16 on 14 and 15 January 2020) indicate the presence of finer particles in the atmosphere.

Further, we have shown volume size distribution (there are some gaps in data on some days) of AOD at Manila AERONET station (Figure 7a). Before the eruption of the Taal, the presence of coarse particles was observed on 7 January 2020, which could be related to local dust mass (coarse particle size); however, on 16 and 19 January 2020, maxima peak was observed for the finer particles associated with the volcanic eruption. Higher AOD (1.27) and higher AE (1.55) were observed on 29 January 2020 (Figure 6b) along with a peak towards the finer particles at Manila station (Figure 7a), which was more prominent in comparison to the other days. The high volume of the fine particles was observed a few days after the volcanic eruptions depending upon the meteorological parameters. The coarser particles also reached Manila stations (67 km areal distance from Taal Volcano) on 21 January 2020. The concentrations of particles (fine and coarse) depend on the Taal eruption and meteorological conditions. It is difficult to estimate these unless one has high spatial and temporal ground and satellite data. The analysis of wind direction shows that westerly winds bring volcanic airmass to Manila and its surroundings, which leads to changes in aerosol properties (Figure 5). Figure 7b shows the wavelength dependence of SSA during January 2020. On 7 January 2020, the mean SSA is close to 0.9, which shows the effect of mixed aerosols due to local sources of emissions. On 16 January 2020, higher SSA is observed at lower wavelengths and low SSA at longer wavelengths, which indicates the presence of finer particles (volcanic plume), and a low value of SSA shows the absorbing nature of aerosols (lower than 0.90). A similar pattern is also observed on 19 January 2020, with the higher SSA when compared to 16 January 2020, i.e., the aerosols are more reflecting in nature. During 22–28 January 2020, SSA is comparatively low and constant but on 29 January 2020, higher SSA value is observed again at a lower wavelength (lower values in infrared band), i.e., particles are finer, the average value of SSA is higher than 0.90, which means particles are reflecting in nature, which is characteristics of SO₂. The changes in SSA clearly show emissions of volcanic ash, which was not regular after the volcanic event on 12 January 2020 and its transport (Figure 7b)

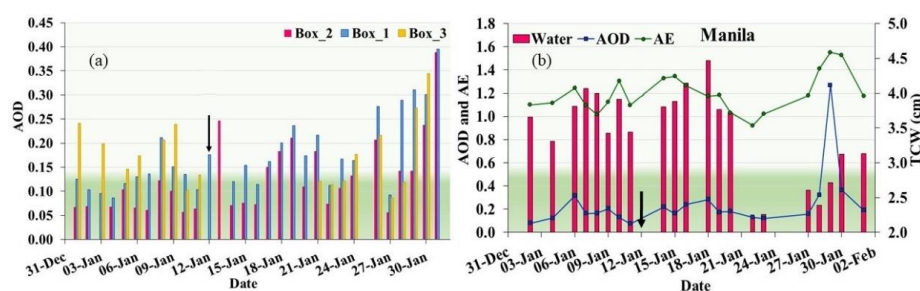


Figure 6. (a) Temporal variations of aerosol optical depth (AOD) over Boxes 1, 2, and 3 during January 2020 using Aqua and Terra MODIS data. (b) Temporal variations of AOD, AE, and TCW at the Manila AERONET station (b). The black downward arrow is the day of the volcanic eruption.

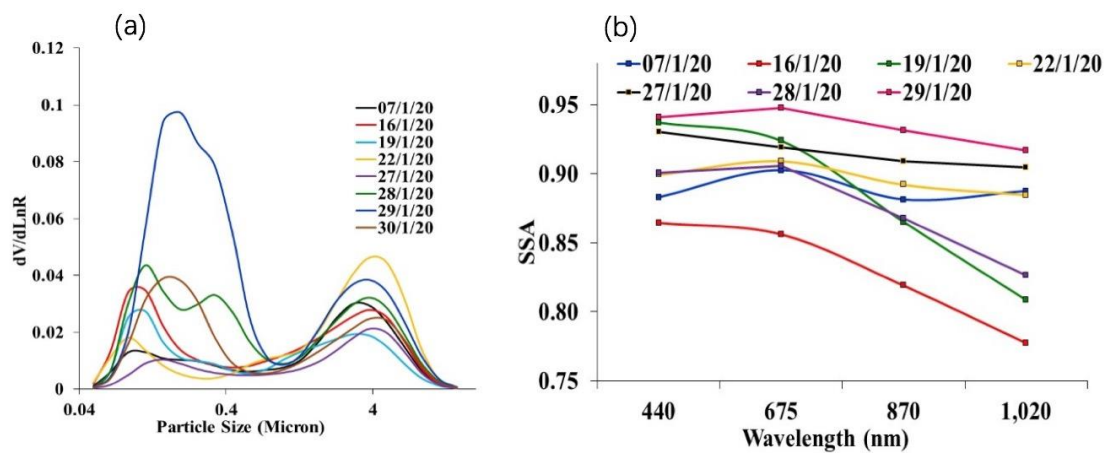


Figure 7. (a) The volume size distribution of aerosols. (b) Wavelength dependence of single scattering albedo (SSA) over Manila AERONET station during January 2020.

4.2. Emission of volcanic gases

Volcanic gases are important products of volcanic activities. We have analyzed SO_2 , Ozone, and CO data observed from satellites before and after the Taal volcano eruption.

4.2.1. SO_2

SO_2 emission from volcanoes is well known. Intense volcanic emission of SO_2 and transport of volcanic ash was observed during and after the Taal volcano eruption (source—newsletter issued by PHIVOLCS) (<https://volcano.si.edu/volcano.cfm?vn=273070>). The SO_2 and volcanic ash were spread around the Taal volcano. We considered the total column of SO_2 observed by OMI and TROPOMI with different spatial resolutions. These two kinds of data are more sensitive to SO_2 at the upper troposphere and the lower stratosphere compared with those retrieving SO_2 products based on thermal infrared measurements, such as IASI (Infrared Atmospheric Sounding Interferometer) and MODIS [64,72]. The OMI SO_2 dataset is used for temporal analysis and TROPOMI for spatial variations. The average OMI SO_2 is found to be 0.13, 0.27, and 0.23 DU (Dobson Unit) over Boxes 1, 2, and 3, respectively. For Box 1, SO_2 data is unavailable between 13 and 19 January 2020. Over Boxes 2 and 3, a sharp rise in SO_2 concentration is observed on 14 January 2020, with about 1.39 and 1.02 DU associated with the volcanic emission, which is higher than the mean value for January 2020 (Figure 8). During the same period in 2018 and 2019, SO_2 concentration (DU) was lower compared to the year 2020. Over Box 2, SO_2 values in 2018 and 2019 were both 0.12 DU, and over Box 3, the SO_2 value in 2018 was 0.55 DU compared to 0.17 DU in 2019. Higher values over Box 3 in 2018 were due to the volcanic eruption on 23 January 2018 in Mount Mayon Volcano, Philippines (<https://www.forbes.com/sites/trevornace/2018/01/22/mount-mayon-volcano-eruption-update-philippines/#31fc8f393796>).

The spatial distribution of enhanced SO_2 from Sentinel-5P TROPOMI is shown in Figure 9. The highest total vertical column of SO_2 appeared one day after the eruption and distributed along the northeast and the southwest. The strongest SO_2 emission (larger than 30 DU) on 13 January 2020 distributed over the Philippine Sea, northeast of the Taal volcano, which coincided with the forward trajectory of air mass at a higher altitude (Figure 4ii,iii) showing the sensitivity to the upper troposphere. Also, the obvious enhancement in SO_2 appeared in the surrounding region of the southwest of Taal. On 14 January, the enhanced SO_2 moved to the south-west and distributed over the ocean, with a lower value (less than 20 DU) compared to the preceding day. Enhanced SO_2 disappeared on 15 January 2020, from the Taal volcano, emissions of gases were intermittent, not continuous, which is supported from the variability in SO_2 concentrations. The earthquake occurrences were frequent on 12 and 13 January 2020, and afterward, few earthquakes occurred. The observed earthquakes were induced from volcanic eruptions, so obviously frequent earthquakes were observed on 12 and 13 January 2020, and

afterward, the volcanic eruption was stopped. This observation clearly supports the observed low emissions of SO₂ after two days of eruptions.

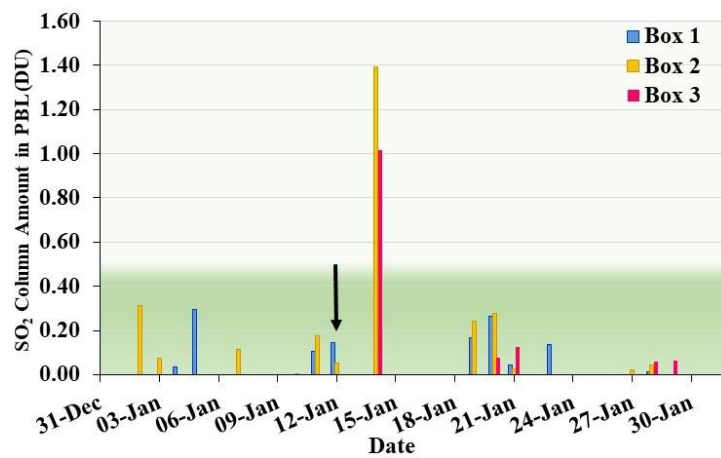


Figure 8. Temporal variations of Total Column SO₂ over Boxes 1 – 3 using OMI measurements. A sharp rise in SO₂ is observed over Boxes 2 and 3 on 14 January, and the volcanic eruptions started on 12 January 2020 (the black arrow points at the date of the volcanic eruption).

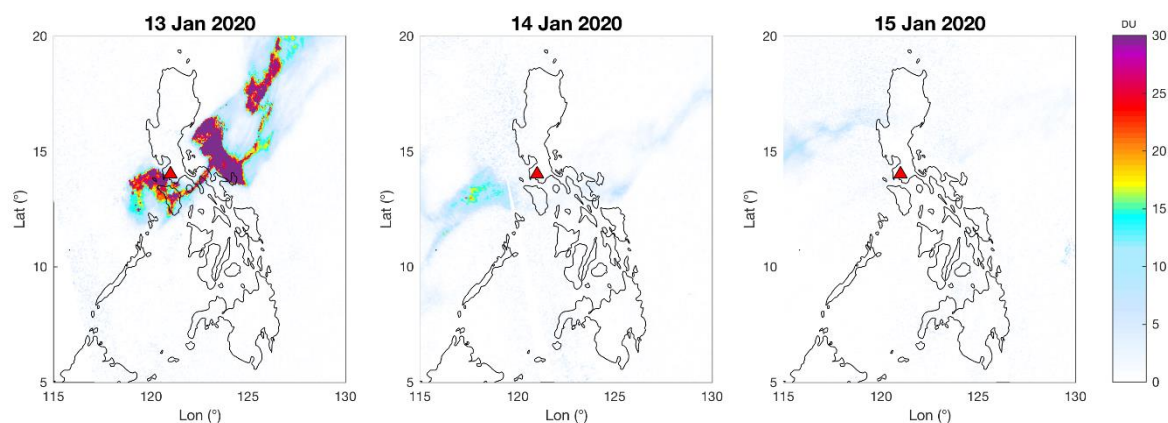


Figure 9. Spatial distribution of the total vertical column of TROPOMI SO₂ after the eruption of the Taal volcano observed by Sentinel-5P. The red triangle indicates the geographic location of the Taal volcano.

4.2.2. Ozone

We have also analyzed the changes in total column ozone (TCO) over Box 1 to 3 around the Taal region.

The TCO observed by AIRS was low on 12 and 13 January 2020 over the three boxes (Figure 3). Afterward, TCO was found to be enhanced (Figure 10a), corresponding to the increase in SO₂ due to the Taal eruption (Figures 8 and 10a). During the initial eruption, the higher SO₂ concentration affected the TCO (due to chemical reaction with atmospheric chlorine). Similar results were also observed with volcanic eruptions elsewhere [8,73–75]. Variations of SO₂ concentrations over Box 1-3 are related to the amount of SO₂ emissions, thus, showing corresponding variations in TCO (Figure 10a). Variations of SO₂ over Box 1-3 (Figure 8) depend on the wind directions, showing changes in TCO (Figure 10a). We also analyzed the spatial variations of TCO from TROPOMI Ozone data, and an obvious decrease has been observed over the Taal volcano region on 13 January 2020 (Figure 10b).

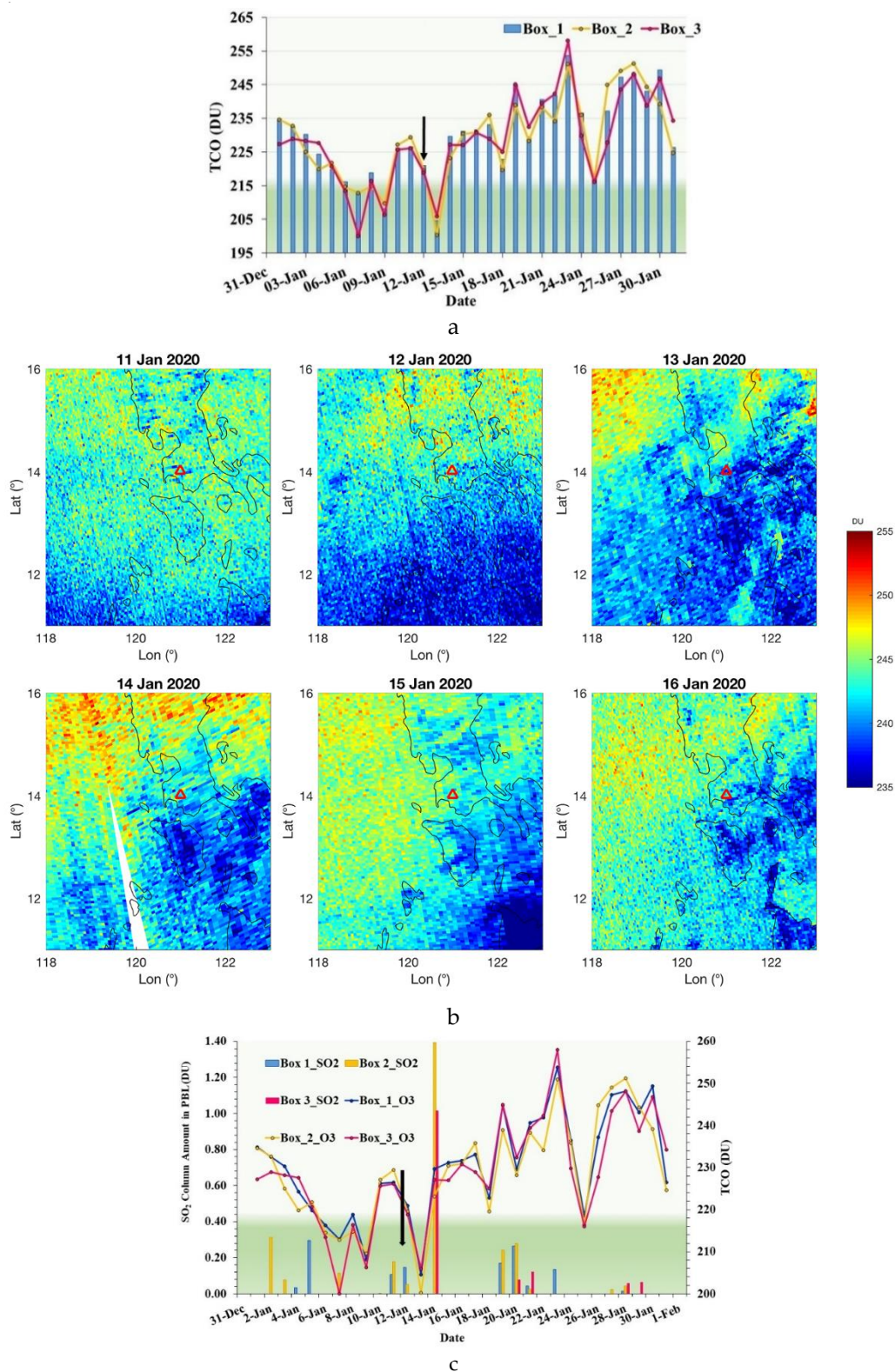


Figure 10. (a) Temporal variations of Total Column Ozone (TCO) observed by an Atmospheric Infrared Sounder (AIRS) over Box 1 to 3 during January 2020. The downward black arrow shows the day of the volcanic eruption. (b) Spatial distribution of the total vertical column of TROPOMI Ozone from 11 to 16 January 2020 around the Taal region observed by Sentinel-5P. The red triangle indicates the geographic location of the Taal volcano. (c) Temporal variations of SO₂ and TCO over Box 1 to 3 for the period 1–31 January 2020. The downward black arrow shows the day of the Taal volcano eruption.

Figure 10c shows variations of SO₂ and TCO over Box 1 to 3 for the period 1–31 January 2020, and the downward black arrow shows the day of the Taal volcano eruption. Prior to the Taal eruption, a seasonal decline (winter season, January) in TCO is observed. After the Taal eruption on 12 January 2020, a peak in SO₂ injection in the planetary boundary layer is observed, which shows increasing values in TCO with strong variability corresponding to SO₂ emissions from the Taal volcano, which appear to decline as SO₂ emissions cease. Such emissions of SO₂ have a long term impact showing a decline in TCO (TCO appears to decline after 31 January 2020, which is also observed in the case of other volcanic eruptions) [8,73–75].

4.2.3. CO

CO is another common volcanic degassing product [34], which could be determined by ground observation [76,77]. In 2012, it was first observed in the Eyjafjallajökull 2010 and Grímsvötn 2011 eruptions in Iceland using satellite data [39], which motivated us to carry out the analysis of Sentinel-5P TROPOMI CO data with a spatial resolution of 5.5×7 km. A slight increase in CO concentrations (Figure 11a) was observed over the Taal volcano region on 14 and 15 January 2020 (not enough data are available on 13 January over this region). AIRS CO mole fraction vertical profile over the Taal region ($2 \times 2^\circ$) also shows similar variations, though it has a low spatial resolution (Figure 11b). An increase in CO mole fraction appeared between 13 and 17 January 2020, soon after the eruption of the Taal volcano, especially at the pressure levels 500–1000 hPa.

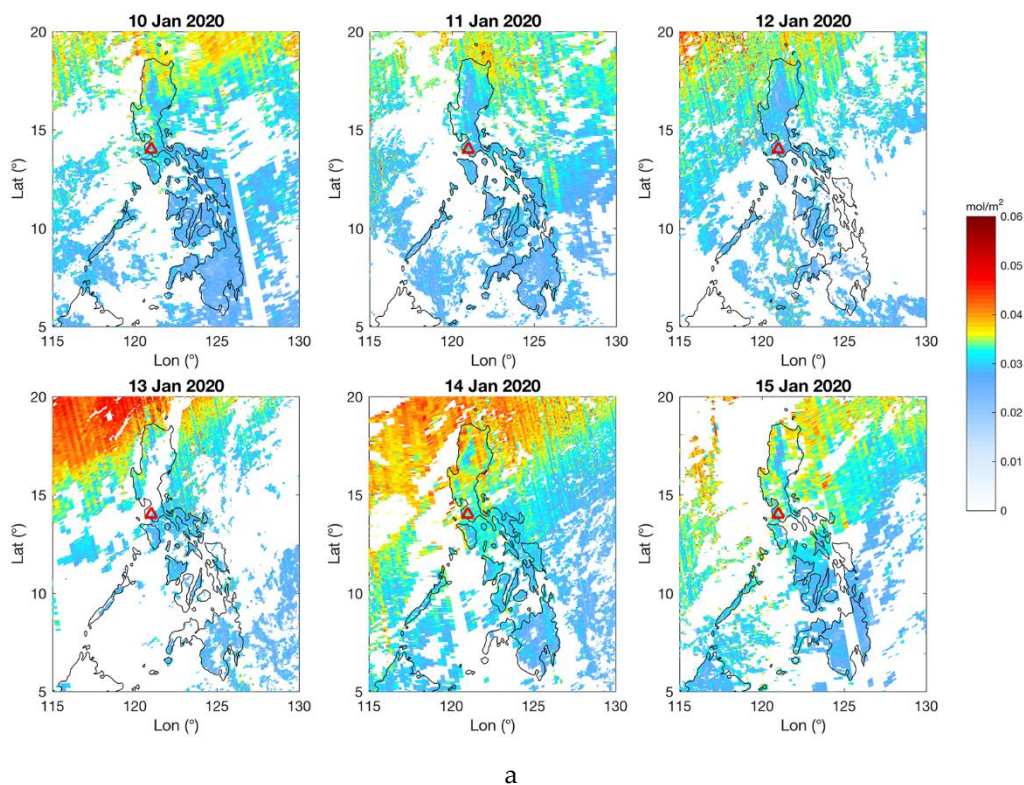


Figure 11. Cont.

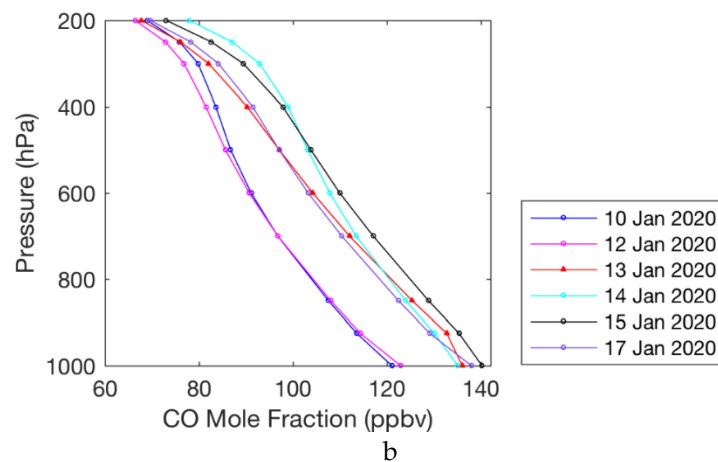


Figure 11. (a) Spatial distribution of the total vertical column of TROPOMI carbon monoxide (CO) before and after the eruption of the Taal volcano observed by Sentinel-5P. The red triangle indicates the geographic location of the Taal volcano. (b) AIRS CO mole fraction vertical profile around the time of the eruption of the Taal volcano.

4.2.4. Water vapor

Water vapor mixing ratio and relative humidity along vertical profiles (Figure 12) over the Taal region ($2 \times 2^\circ$) observed by AIRS before and after the eruption of the Taal volcano have been considered. An obvious enhancement in both water vapor and relative humidity occurred on 12 and 13 January 2020 at the pressure levels 200–400 hPa compared to other days, which indicates the enhancements of the water mixing ratio and relative humidity in the upper troposphere. The enhanced water vapor could also cause an ozone decrease (Figure 10a,b) [78]. With the injection of hot gases from volcanic eruptions, the water vapor and relative humidity enhanced at pressure levels 850–1000 hPa on 13 January 2020, showing a pronounced increase compared with 12 January 2020.

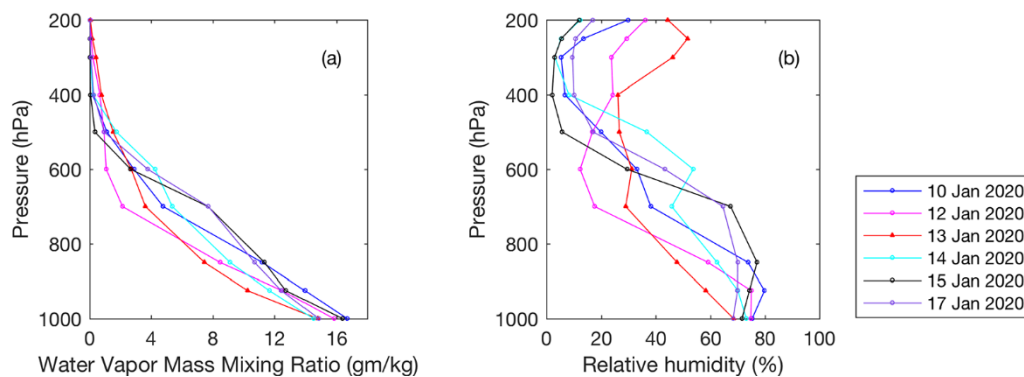


Figure 12. Vertical profiles before and after the eruption of the Taal volcano. (a) AIRS water vapor mixing ratio. (b) Relative humidity.

4.3. Changes in Ocean Parameters

4.3.1. Salinity and temperature

The vertical distributions of ocean salinity from three Argo stations have been analyzed (Figure 13). Station [2902753] is in the north-eastern direction of Taal, and stations [2902784] and [2902786] are to the south-west of the volcano (Figure 3). Station [2902784] is found to be in the direct path of the air mass trajectory, and station [2902786] is not very influenced by the volcanic eruptions. At station [2902753], salinity was higher on 7 January and later shows a decrease on the surface of the water, but the change is small. At station [2902784] (on the route of air mass transportation), the highest salinity

close to the surface was found on 14 January 2020, and later on, a decrease in salinity at the depth levels between 0 and 20 m was observed. This decrease in ocean salinity is likely due to the intense deposition of thick ash, which was even observed on the roofs of houses (personal communication with Saroj Panda currently living in Manila and <https://volcano.si.edu/volcano.cfm?vn=273070>). For station [2902786], salinity was also higher close to the water surface on 13 January at similar depths, but at this station, the highest salinity was found on 27 January 2020. The salinity was found to be similar after a depth of 100 m at these two stations.

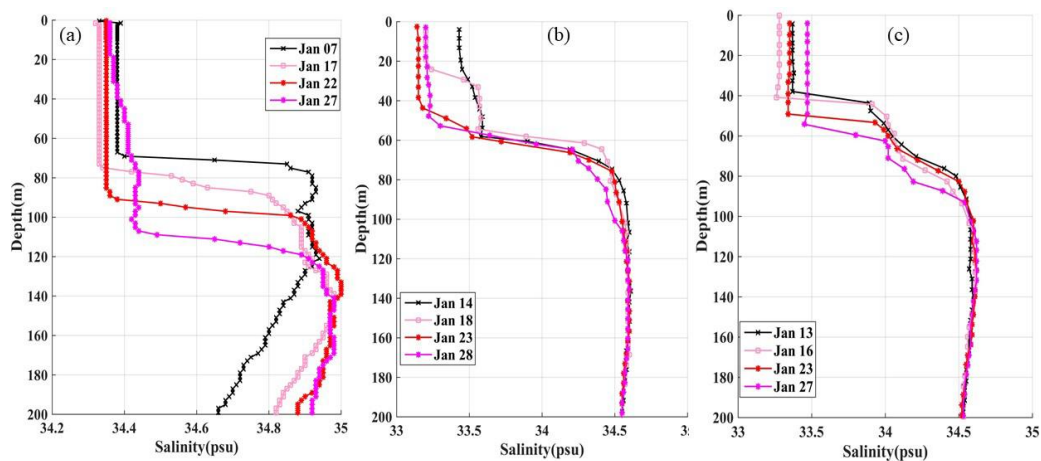


Figure 13. Vertical profiles of salinity at three Argo stations (a) 2902753, (b) 2902784, and (c) 2902786 around the time of the eruption of the Taal volcano.

We have also analyzed the vertical profiles of water temperature up to a 200 m (200 decibar pressure level) depth of the three Argo stations (Figure 14). At station [2902753], on 7 January 2020, the water temperature was higher up to the depth of 70 m, and the temperature was lowest at depths greater than 70 m. The temperature in deeper water at this station increased gradually until the end of the month (no data is available for 13 to 14 January 2020 for this station). At stations [2902784] and [2902786], a reduction in the shallow water temperature was observed on 14 and 13 January, respectively; later, a gradual rise in temperature was observed. An obvious variation in shallow water temperature was observed at station [2902784] because it is in the path of volcanic air mass transportation and was influenced by particle deposition.

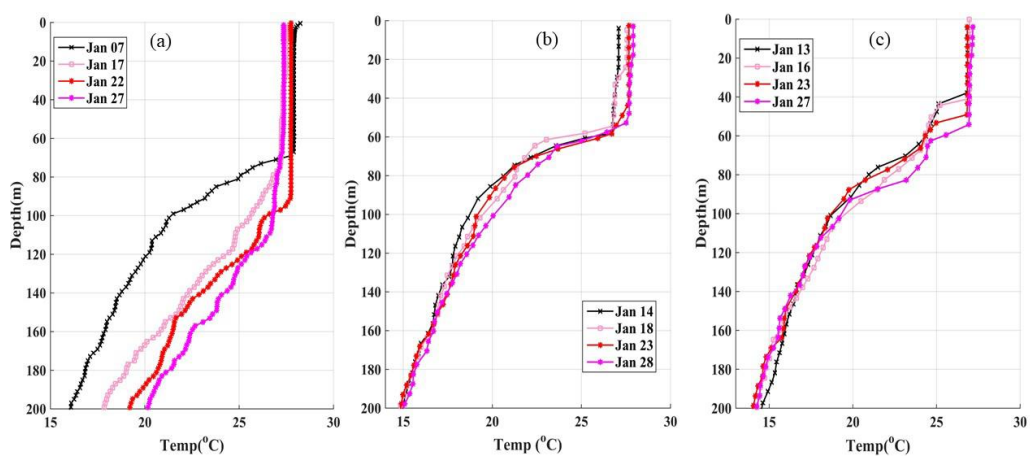


Figure 14. Vertical profiles of temperature at three Argo stations (a) 2902753, (b) 2902784, and (c) 2902786 around the time of the eruption of the Taal volcano.

Temporal variations of sea surface temperature (SST) were analyzed for a sub-selected region between 13° N -15 °N latitudes and 120° E -122 °E longitudes. For this purpose, Multi-scale Ultra-high Resolution (MUR) level-4 (L4) gap-free SST analysis data were obtained from NASA's JPL Physical Oceanography Distributed Active Archive Center (https://podaac.jpl.nasa.gov/Multi-scale_Ultra-high_Resolution_MUR-SST). The temporal variation of SST was visualized here, for the period of 1 January to 16 February 2020, and additionally, with respect to climatological monthly average SST. The aim was to study any sharp changes in SST, relatively, and therefore the true value of SST is not relevant for this qualitative study. The MUR analysis product uses a variety of input SSTs and provides a grid resolution of ~1 km, yielding about 21,900 points daily, for the sub-selected area of the study.

Figure 15 shows the temporal variations of the SST (Y1 axis) and SST anomaly (Y2 axis). The mean SST anomaly shows a decrease in SST after the volcanic eruption until 16 January 2020, which is likely due to the fall of volcanic ashes, and after a few days, the SST increased. The mean SST shows a pronounced decline after January 2020, which is likely due to the spread of volcanic ashes over the ocean water surface, which is also evident from the observed decline in the ocean water temperature and salinity from Argo floats at the end of January (27) 2020.

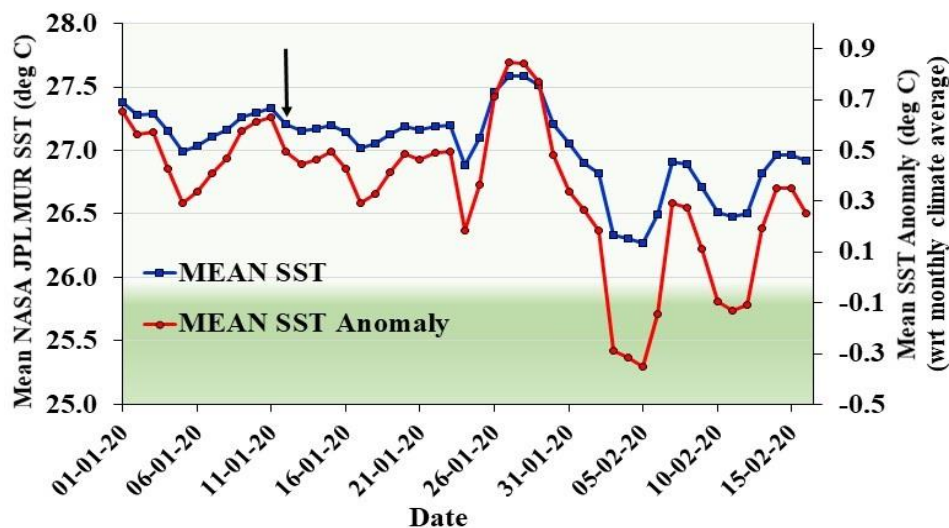


Figure 15. Time series of sea surface temperature (SST) and SST anomaly over the Taal volcano and surroundings (Latitude: 13 °N - 15 °N; Longitude: 120°E - 122 °E). The downward black arrow shows the day of the volcanic eruption.

4.3.2. Surface latent heat flux (SLHF)

Surface latent heat flux (SLHF) is an important parameter, reflecting the energy transportation between the ocean and the atmosphere. Higher SLHF is always observed at the ocean–land interface due to the high exchange of water vapor and heat with the atmosphere [79]. Considering the Taal volcano is surrounded by ocean, SLHF data are used to study the heat exchange over the surrounding atmosphere–ocean region around the time of the Taal volcano eruption. The SLHF dataset is obtained from the NCEP/NCAR (National Centers for Environmental Prediction/National Center for Atmospheric Research) reanalysis with a spatial resolution of 1.875° at longitude and an approximately 1.9° at latitude [80]. Figure 16 shows spatial distributions of daily SLHF around the Taal volcano for the period 8 - 16 January 2020. An enhancement in SLHF is observed over the ocean, about 400 km south-west of the Taal volcano, between 12 and 14 January 2020. The highest enhancement appears on 13 January 2020, one day after the volcanic eruption.

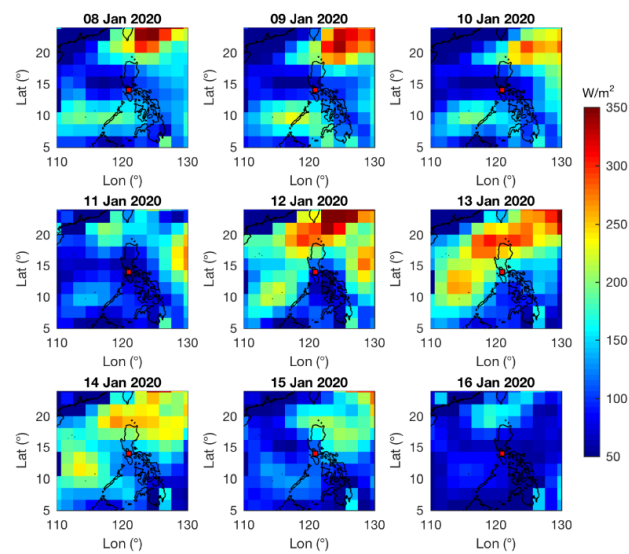


Figure 16. Spatial variations of surface latent heat flux (SLHF) around the region of the Taal volcano between 8 and 16 January 2020. The red square indicates the Taal volcano.

Further, we have considered SLHF variations at different times 00, 06, 12, and 18 UTC daily. Figure 17 shows spatial variations of SLHF at 00, 06, 12, and 18 UTC for the periods 11 to 13 January 2020. An obvious variation occurred on the southwest of the Taal volcano, which is on the path of volcanic air mass transportation at a lower altitude (Figure 4i). The increased SLHF is observed from 12 UTC, on 12 January 2020, six hours after the start of the eruption. The highest value appeared at 06 UTC on 13 January 2020. Temporal variations of the enhanced SLHF region have also been analyzed (Figure 18). The distinct SLHF enhancement has been observed after the Taal volcano eruption, which was recovered on 15 January 2020 (Figure 18). The highest value of 264.2 W/m^2 occurred at 06 UTC on 13 January 2020. We have also observed the high SLHF values in the north-east of the Taal volcano during this period, which could be attributed to the influence of Kuroshio flows during the winter season [81].

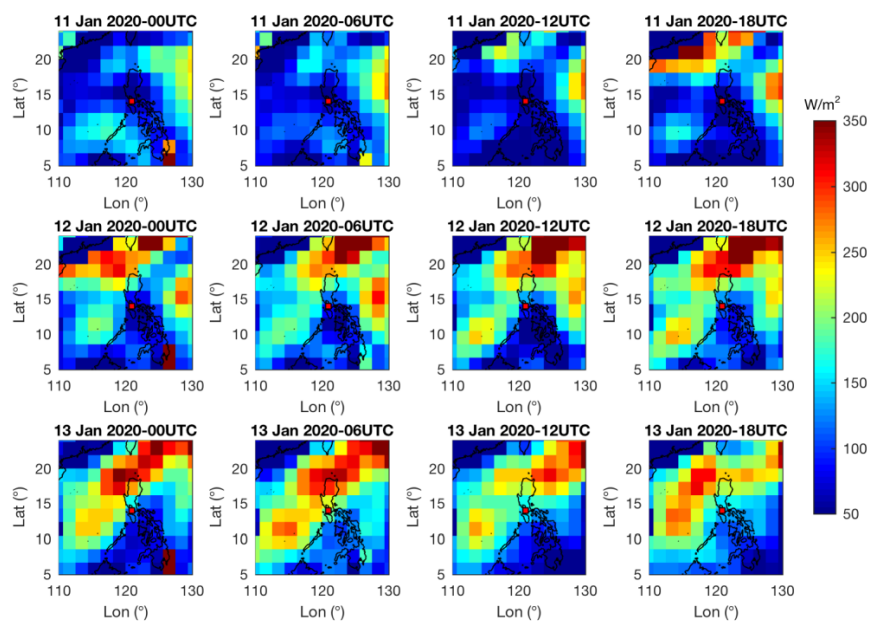


Figure 17. Spatial variations of surface latent heat flux at 00, 06, 12, and 18 UTC around the Taal volcano from 11 to 13 January 2020. The red square indicates the Taal volcano.

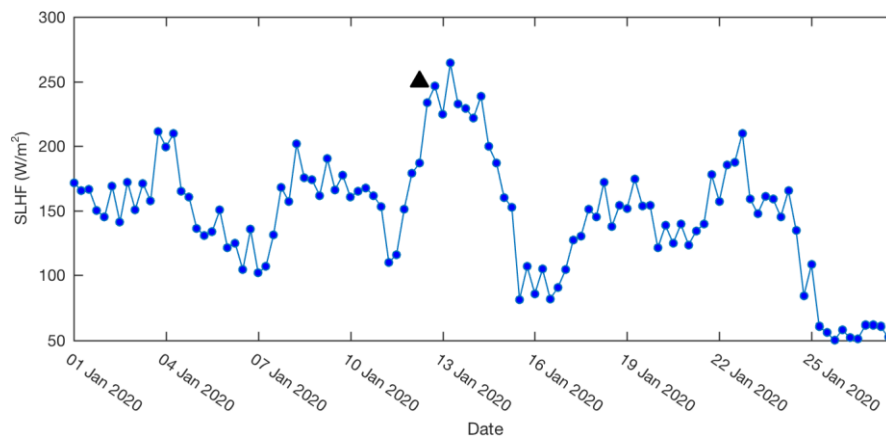


Figure 18. Temporal variations of 4-time daily SLHF over the ocean located on the southwest of the Taal volcano before and after the eruption. The black upward triangle shows the time of the volcanic eruption.

5. Discussion

The ash plume from the Taal volcanic eruption spreads in the surroundings of the Taal volcano, and the maximum ash plume spread is in the south-west, which is also evident from the wind rose diagram (Figure 5). The volcanic eruptions triggered earthquakes, and an increase in the frequency of earthquakes (Figure 2a,b) was observed from the beginning of eruptions, with a few medium-sized earthquakes (magnitude greater than 4.0 mb) also observed (Figure 2c). The emissions of gases and volcanic ash began with the volcanic eruptions, which were dispersed around Taal guided by the wind directions near the surface and at the different altitudes. The volcanic ash reached up to 14.5 km altitude in the atmosphere, which was spread in the north-east directions from the Taal volcano [50] (https://so2.gsfc.nasa.gov/omps_2012_now.html#2020). The aerosol concentrations enhanced in the atmosphere over Taal and its surroundings. Higher values of AOD and high AE have been observed at Manila under the influence of the western and south-west winds. Higher AOD shows an increase in atmospheric pollution affecting air quality, and larger values of AE show the presence of smoke/ashes (Figure 6), which is also reflected from the increase in the volume size distribution of the small radius of particles (finer particles) (Figure 7a) after the eruption. A small increase in the volume of coarser particles was also observed from AERONET station at Manila. A decreasing trend of SSA with wavelength from the AERONET Manila station clearly shows the presence of volcanic ashes (Figure 7b). We observed the rapid decrease in ozone while SO_2 increased one day after the eruption of the Taal volcano (Figures 9 and 10a). That could be attributed to the discharging of significant emissions of reactive halogen that existed in volcanic plumes. The high correlation between SO_2 and halogen monoxides provided evidence for the volcanic origin of the reactive halogen species [82]. The self and cross-reactions of reactive halogen yield the destruction of ozone in the vicinity of the volcano (Figure 10a,b) [83]. The enhancement of water vapor in the upper troposphere has been observed after the volcanic eruption (Figure 12). The concentration and distribution of water vapor and ozone are sensitive to both chemical processes, such as cloud microphysics and transport processes influencing the convection and stratosphere–troposphere exchange (STE) [84]. These processes influence the ozone concentrations and contribute to a warming of the tropopause, which allows higher water vapor concentrations to enter the stratosphere. Higher stratospheric water vapor coupled with stratospheric cooling induced by increases in atmospheric carbon dioxide can lead to increases in stratospheric ozone depletion. We observed an obvious variation of SLHF after the volcanic eruption, which could be related to the impact of volcanic ashes, but the mechanism still needs to be examined further.

6. Conclusion

We have analyzed the optical properties of volcanic aerosols, volcanic gas emission, and ocean parameters around the time of the eruption of the Taal volcano on 12 January 2020 using a combination of satellite and ground observations. Changes in aerosol optical depth (AOD) in the western and south-western regions after the Taal volcano eruption have been observed using MODIS AOD data and are likely to be associated with the transport of air mass as reflected by the forward trajectory analysis and wind directions. AOD, Angstrom Exponent (AE), aerosol size distribution (ASD), and single scattering albedo (SSA) acquired from the AERONET Manila station (67 km areal distance from the Taal volcano) indicated the presence of finer particles (volcanic ash plume). The results combined with satellite and ground observations suggest that the eruption of a volcano strongly influences the optical properties of aerosols. We have also observed pronounced variations in volcanic degassing based on different satellite observations with various spatial resolutions. An obvious enhancement in SO₂ appeared on 13 January 2020 in the surrounding region of the southwest of the Taal volcano. Also, a decline in ozone has been observed on the same day in the western region, which could be due to the chemical reaction of SO₂ and chlorine in the atmosphere. We have also observed enhanced CO, water vapor, and relative humidity in the troposphere. The observed changes show evidence of a strong tropospheric–stratospheric exchange affecting the total column ozone (TCO). The unusual variations in salinity, sea temperature, and surface latent heat flux have also been found as a result of the westward air mass at a lower altitude from the Taal volcano over the ocean. Especially, some ocean parameters could be changed while volcanic ash reaches over the ocean and is deposited. Within a 20 km radius of the Taal volcano, thick ashes were deposited over the roofs of houses (PHIVOLCS, <https://volcano.si.edu/volcano.cfm?vn=273070>). The impact of the eruption was observed in the south-west direction from the volcanic ash at lower altitudes, whereas the changes were more prevalent in the north-east direction due to south-westerly winds at a higher altitude. The integrated approach combining multi-satellite observations, Argo measurements, AERONET data, and HYSPLIT trajectories provides valuable information to study the changes in atmospheric and meteorological parameters, and such an approach may be used to study volcanic eruptions and to study the areal extent of the volcanic ash from volcanos.

Author Contributions: The present study is the effort of all the authors. The idea of the work was started by R.P.S., and the analysis of data was carried out by all the authors. The original draft was prepared by F.J., A.C., and R.P.S., and the draft was reviewed by R.P.S. and P.D. All authors have read and agreed to the published version of the manuscript.

Funding: This research was funded by the National Natural Science Foundation of China (Grant NO. 41604062) and the Basic Research Project of Institute of Earthquake Forecasting, CEA (Grant NO. 2017IES0403).

Acknowledgments: The authors are grateful to USGS, NOAA, NASA Giovanni team, TROPOMI, NOAA HYSPLIT, PHIVOLCS, and NASA AERONET teams for data availability. We are also grateful to the PHIVOLCS organization and EMSEV IUGG Commissions, especially Toshi Nagoya, for sharing the EMSEV report. The views, opinions, and findings contained in this paper are those of the authors and should not be construed as an official Colorado State University, NOAA, or US Government position, policy, or decision. The authors thank the four reviewers for their comments and suggestions that helped us to improve the earlier version of the manuscript.

Conflicts of Interest: The authors declare no conflict of interest.

References

1. Lu, Z.; Dzurisin, D. *Natural Hazards: Earthquakes, Volcanoes, and Landslides. Radar Monitoring of Volcanic Activities*; CRC Press: Boca Raton, FL, USA, 2018; pp. 421–446.
2. Kasatkina, E.A.; Shumilov, O.; Timonen, M.; Kanatjev, A.G. Impact of powerful volcanic eruptions and solar activity on the climate above the Arctic Circle. *Geofis. Int.* **2018**, *57*, 67–77. [[CrossRef](#)]
3. Hlodversdottir, H.; Pétursdóttir, G.; Carlsen, H.K.; Gislason, T.; Hauksdóttir, A. Long-term health effects of the Eyjafjallajökull volcanic eruption: a prospective cohort study in 2010 and 2013. *BMJ Open* **2016**, *6*, e011444. [[CrossRef](#)] [[PubMed](#)]

4. Schmidt, A.; Witham, C.; Theys, N.; Richards, N.A.D.; Thordarson, T.; Szpek, K.; Feng, W.; Hort, M.C.; Woolley, A.M.; Jones, A.R.; et al. Assessing hazards to aviation from sulfur dioxide emitted by explosive Icelandic eruptions. *J. Geophys. Res. Atmos.* **2014**, *119*. [[CrossRef](#)]
5. Guðmundsson, G.; Finnbjörnsdóttir, R.G.; Johannsson, T.; Rafnsson, V. Air pollution in Iceland and the effects on human health. Review. *Laeknabladid* **2019**, *105*, 443–452.
6. Möller, R.; Dagsson-Waldhauserova, P.; Möller, M.; Kukla, P.A.; Schneider, C.; Gudmundsson, M.T. Persistent albedo reduction on southern Icelandic glaciers due to ashfall from the 2010 Eyjafjallajökull eruption. *Remote Sens. Environ.* **2019**, *233*. [[CrossRef](#)]
7. Reichardt, U.; Ulfarsson, G.F.; Pétursdóttir, G. Developing scenarios to explore impacts and weaknesses in aviation response exercises for volcanic ash eruptions in Europe. *J. Air Transp. Manag.* **2019**, *79*. [[CrossRef](#)]
8. Bird, D.; Jóhannesdóttir, G.; Reynisson, V.; Karlsdóttir, S.; Gudmundsson, M.T.; Gísladóttir, G. Crisis coordination and communication during the 2010 Eyjafjallajökull eruption. In *Observing the Volcano World*; Springer: Berlin/Heidelberg, Germany, 2017.
9. Yeloff, D.; Mauquoy, D.; Barber, K.; Way, S.; Van Geel, B.; Turney, C.S.M. Volcanic Ash Deposition and Long-Term Vegetation Change on Subantarctic Marion Island. *Arctic. Antarct. Alp. Res.* **2007**, *39*, 500–511. [[CrossRef](#)]
10. Stenchikov, G.; Delworth, T.L.; Ramaswamy, V.; Stouffer, R.J.; Wittenberg, A.T.; Zeng, F. Volcanic signals in oceans. *J. Geophys. Res. Space Phys.* **2009**, *114*. [[CrossRef](#)]
11. Gleckler, P.J.; AchutaRao, K.; Gregory, J.; Santer, B.D.; Taylor, K.E.; Wigley, T.M.L. Krakatoa lives: The effect of volcanic eruptions on ocean heat content and thermal expansion. *Geophys. Res. Lett.* **2006**, *33*. [[CrossRef](#)]
12. Wu, X.; Griessbach, S.; Hoffmann, L. Equatorward dispersion of a high-latitude volcanic plume and its relation to the Asian summer monsoon: A case study of the Sarychev eruption in 2009. *Atmospheric Chem. Phys. Discuss.* **2017**, *17*, 13439. [[CrossRef](#)]
13. Schmidt, A.; Leadbetter, S.; Theys, N.; Carboni, E.; Witham, C.; Stevenson, J.A.; Birch, C.E.; Thordarson, T.; Turnock, S.; Barsotti, S.; et al. Satellite detection, long-range transport, and air quality impacts of volcanic sulfur dioxide from the 2014–2015 flood lava eruption at Bárðarbunga (Iceland). *J. Geophys. Res. Atmos.* **2015**, *120*, 9739–9757. [[CrossRef](#)]
14. Kim, S.; Lee, J.; Oh, S.; Yoon, Y. Assessment of the volcanic hazard of Mt. Paektu explosion to international air traffic using South Korean airspace. *Nat. Hazards* **2019**, *96*, 647–667. [[CrossRef](#)]
15. Casadevall, T.J. The 1989–1990 eruption of Redoubt Volcano, Alaska: Impacts on aircraft operations. *J. Volcanol. Geotherm. Res.* **1994**, *62*, 301–316. [[CrossRef](#)]
16. Soden, B. Global Cooling After the Eruption of Mount Pinatubo: A Test of Climate Feedback by Water Vapor. *Science* **2002**, *296*, 727–730. [[CrossRef](#)]
17. Xiao, N.; Li, J. Mechanism of stratospheric decadal abrupt cooling in the Early 1990s as influenced by the Pinatubo eruption. *Chin. Sci. Bull.* **2011**, *56*, 772–780. [[CrossRef](#)]
18. Furtney, M.A.; Pritchard, M.; Biggs, J.; Carn, S.A.; Ebmeier, S.K.; Jay, J.A.; Kilbride, B.T.M.; Reath, K.A. Synthesizing multi-sensor, multi-satellite, multi-decadal datasets for global volcano monitoring. *J. Volcanol. Geotherm. Res.* **2018**, *365*, 38–56. [[CrossRef](#)]
19. Oppenheimer, C. Remote sensing of the colour and temperature of volcanic lakes. *Int. J. Remote. Sens.* **1997**, *18*, 5–37. [[CrossRef](#)]
20. Smets, B.; D'Oreye, N.; Kervyn, F.; Kervyn, M.; Albino, F.; Arellano, S.; Bagalwa, M.; Balagizi, C.; Carn, S.A.; Darrah, T.H.; et al. Detailed multidisciplinary monitoring reveals pre- and co-eruptive signals at Nyamulagira volcano (North Kivu, Democratic Republic of Congo). *Bull. Volcanol.* **2013**, *76*, 787. [[CrossRef](#)]
21. Corradini, S.; Montopoli, M.; Guerrieri, L.; Ricci, M.; Scollo, S.; Merucci, L.; Marzano, F.S.; Pugnaghi, S.; Prestifilippo, M.; Ventress, L.J.; et al. A Multi-Sensor Approach for Volcanic Ash Cloud Retrieval and Eruption Characterization: The 23 November 2013 Etna Lava Fountain. *Remote. Sens.* **2016**, *8*, 58. [[CrossRef](#)]
22. Oppenheimer, C. Lava flow cooling estimated from Landsat Thematic Mapper infrared data: The Lonquimay Eruption (Chile, 1989). *J. Geophys. Res. Space Phys.* **1991**, *96*, 21865–21878. [[CrossRef](#)]
23. Pergola, N.; Marchese, F.; Tramutoli, V. Automated detection of thermal features of active volcanoes by means of infrared AVHRR records. *Remote. Sens. Environ.* **2004**, *93*, 311–327. [[CrossRef](#)]
24. Marchese, F.; Falconieri, A.; Pergola, N.; Tramutoli, V. A retrospective analysis of the Shinmoedake (Japan) eruption of 26–27 January 2011 by means of Japanese geostationary satellite data. *J. Volcanol. Geotherm. Res.* **2014**, *269*, 1–13. [[CrossRef](#)]

25. Marchese, F.; Ciampa, M.; Filizzola, C.; Lacava, T.; Mazzeo, G.; Pergola, N.; Tramutoli, V. On the Exportability of Robust Satellite Techniques (RST) for Active Volcano Monitoring. *Remote Sens.* **2010**, *2*, 1575–1588. [[CrossRef](#)]
26. Marchese, F.; Lacava, T.; Pergola, N.; Hattori, K.; Miraglia, E.; Tramutoli, V. Inferring phases of thermal unrest at Mt. Asama (Japan) from infrared satellite observations. *J. Volcanol. Geotherm. Res.* **2012**, *237*, 10–18. [[CrossRef](#)]
27. Poland, M.P. Time-averaged discharge rate of subaerial lava at Kilauea Volcano, Hawai'i, measured from TanDEM-X interferometry: Implications for magma supply and storage during 2011–2013. *J. Geophys. Res. Solid Earth* **2014**, *119*, 5464–5481. [[CrossRef](#)]
28. Negro, C.; Cappello, A.; Ganci, G. Quantifying lava flow hazards in response to effusive eruption. *GSA Bull.* **2015**, *128*, 752–763. [[CrossRef](#)]
29. Del Negro, C.; Cappello, A.; Bilotta, G.; Ganci, G.; Hérault, A.; Zago, V. Living at the edge of an active volcano: Risk from lava flows on Mt. Etna. *GSA Bull.* **2019**. [[CrossRef](#)]
30. Duggen, S.; Croot, P.; Schacht, U.; Hoffmann, L. Subduction zone volcanic ash can fertilize the surface ocean and stimulate phytoplankton growth: Evidence from biogeochemical experiments and satellite data. *Geophys. Res. Lett.* **2007**, *34*. [[CrossRef](#)]
31. Hamme, R.; Webley, P.; DeGrandpre, M.D.; Emerson, S.; Giesbrecht, K.; Gower, J.F.R.; Kavanaugh, M.T.; Pena, A.; Batten, S.D.; Grundle, D.S.; et al. Volcanic ash fuels anomalous plankton bloom in subarctic northeast Pacific. *Geophys. Res. Lett.* **2010**, *37*. [[CrossRef](#)]
32. Westberry, T.; Shi, Y.; Yu, H.; Behrenfeld, M.; Remer, L. Satellite-Detected Ocean Ecosystem Response to Volcanic Eruptions in the Subarctic Northeast Pacific Ocean. *Geophys. Res. Lett.* **2019**, *46*, 11270–11280. [[CrossRef](#)]
33. Bruno, N.; Caltabiano, T.; Giammanco, S.; Romano, R. Degassing of SO₂ and CO₂ at Mount Etna (Sicily) as an indicator of pre-eruptive ascent and shallow emplacement of magma. *J. Volcanol. Geotherm. Res.* **2001**, *110*, 137–153. [[CrossRef](#)]
34. Carn, S.A.; Clarisse, L.; Prata, F. Multi-decadal satellite measurements of global volcanic degassing. *J. Volcanol. Geotherm. Res.* **2016**, *311*, 99–134. [[CrossRef](#)]
35. Khokhar, M.; Frankenberg, C.; Van Roozendaal, M.; Beirle, S.; Kühl, S.; Richter, A.; Platt, U.; Wagner, T. Satellite observations of atmospheric SO₂ from volcanic eruptions during the time-period of 1996–2002. *Adv. Space Res.* **2005**, *36*, 879–887. [[CrossRef](#)]
36. Carboni, E.; Mather, T.; Schmidt, A.; Grainger, R.; Pfeffer, M.A.; Ialongo, I.; Theys, N. Satellite-derived sulfur dioxide (SO₂) emissions from the 2014–2015 Holuhraun eruption (Iceland). *Atmospheric Chem. Phys. Discuss.* **2019**, *19*, 4851–4862. [[CrossRef](#)]
37. Hayer, C.; Wadge, G.; Edmonds, M.; Christopher, T. Sensitivity of OMI SO₂ measurements to variable eruptive behaviour at Soufrière Hills Volcano, Montserrat. *J. Volcanol. Geotherm. Res.* **2016**, *312*, 1–10. [[CrossRef](#)]
38. Theys, N.; Hedelt, P.; De Smedt, I.; Lerot, C.; Yu, H.; Vlietinck, J.; Pedernana, M.; Arellano, S.; Galle, B.; Fernandez, D.; et al. Global monitoring of volcanic SO₂ degassing with unprecedented resolution from TROPOMI onboard Sentinel-5 Precursor. *Sci. Rep.* **2019**, *9*, 2643. [[CrossRef](#)]
39. Martínez-Alonso, S.; Deeter, M.; Worden, H.M.; Clerbaux, C.; Mao, D.; Gille, J.C. First satellite identification of volcanic carbon monoxide. *Geophys. Res. Lett.* **2012**, *39*. [[CrossRef](#)]
40. Prata, F.; Carn, S.A.; Stohl, A.; Kerkmann, J. Long range transport and fate of a stratospheric volcanic cloud from Soufrière Hills volcano, Montserrat. *Atmospheric Chem. Phys. Discuss.* **2007**, *7*, 5093–5103. [[CrossRef](#)]
41. Clarisse, L.; Coheur, P.-F.; Chefdeville, S.; Lacour, J.; Hurtmans, D.; Clerbaux, C. Infrared satellite observations of hydrogen sulfide in the volcanic plume of the August 2008 Kasatochi eruption. *Geophys. Res. Lett.* **2011**, *38*. [[CrossRef](#)]
42. Dubuisson, P.; Herbin, H.; Minvielle, F.; Compiègne, M.; Thieuleux, F.; Parol, F.; Pelon, J. Remote sensing of volcanic ash plumes from thermal infrared: a case study analysis from SEVIRI, MODIS and IASI instruments. *Atmospheric Meas. Tech.* **2014**, *7*, 359–371. [[CrossRef](#)]
43. Corradini, S.; Merucci, L.; Prata, F.; Piscini, A. Volcanic ash and SO₂ in the 2008 Kasatochi eruption: Retrievals comparison from different IR satellite sensors. *J. Geophys. Res. Space Phys.* **2010**, *115*. [[CrossRef](#)]

44. Lagios, E.; Vassilopoulou, S.; Sakkas, V.; Dietrich, V.; Damiata, B.; Ganas, A. Testing satellite and ground thermal imaging of low-temperature fumarolic fields: The dormant Nisyros Volcano (Greece). *ISPRS J. Photogramm. Remote. Sens.* **2007**, *62*, 447–460. [[CrossRef](#)]
45. Zakšek, K.; Hort, M.; Lorenz, E. Satellite and Ground Based Thermal Observation of the 2014 Effusive Eruption at Stromboli Volcano. *Remote. Sens.* **2015**, *7*, 17190–17211. [[CrossRef](#)]
46. McCormick, B.T.; Herzog, M.; Yang, J.; Edmonds, M.; Mather, T.; Carn, S.A.; Hidalgo, S.; Langmann, B. A comparison of satellite- and ground-based measurements of SO₂ emissions from Tungurahua volcano, Ecuador. *J. Geophys. Res. Atmos.* **2014**, *119*, 4264–4285. [[CrossRef](#)]
47. Pardini, F.; Burton, M.; Vitturi, M.M.; Corradini, S.; Salerno, G.; Merucci, L.; Di Di Grazia, G. Retrieval and intercomparison of volcanic SO₂ injection height and eruption time from satellite maps and ground-based observations. *J. Volcanol. Geotherm. Res.* **2017**, *331*, 79–91. [[CrossRef](#)]
48. Rybin, A.; Chibisova, M.; Webley, P.; Steensen, T.; Izbekov, P.; Neal, C.; Realmuto, V. Satellite and ground observations of the June 2009 eruption of Sarychev Peak volcano, Matua Island, Central Kuriles. *Bull. Volcanol.* **2011**, *73*, 1377–1392. [[CrossRef](#)]
49. Poret, M.; Corradini, S.; Merucci, L.; Costa, A.; Andronico, D.; Montopoli, M.; Vulpiani, G.; Freret-Lorgeril, V. Reconstructing volcanic plume evolution integrating satellite and ground-based data: application to the 23 November 2013 Etna eruption. *Atmospheric Chem. Phys. Discuss.* **2018**, *18*, 4695–4714. [[CrossRef](#)]
50. Mallapaty, S. Scientists fear major volcanic eruption in the Philippines. *Nature* **2020**. [[CrossRef](#)]
51. Moore, J.G.; Nakamura, K.; Alcaraz, A. The September 28–30, 1965 eruption of Taal Volcano, Philippines. *Bull. Volcanol.* **1966**, *29*, 75–76. [[CrossRef](#)]
52. Zlotnicki, J.; Sasai, Y.; Toutain, J.P.; Villacorte, E.U.; Bernard, A.; Sabit, J.P.; Gordon, J.M.; Corpuz, E.G.; Harada, M.; Punongbayan, J.T.; et al. Combined electromagnetic, geochemical and thermal surveys of Taal volcano (Philippines) during the period 2005–2006. *Bull. Volcanol.* **2008**, *71*, 29–47. [[CrossRef](#)]
53. Reyes, P.J.D.; Bornas, M.A.V.; Dominey-Howes, D.; Pidlaon, A.C.; Magill, C.; Solidum, J.R.U.; Solidum, R.U. A synthesis and review of historical eruptions at Taal Volcano, Southern Luzon, Philippines. *Earth-Science Rev.* **2018**, *177*, 565–588. [[CrossRef](#)]
54. Kumagai, H.; Niino, M. *Temporal Variations in Seismic Scattering Characteristics in a Shallow S-wave Attenuation Region at Taal Volcano, Philippines*; American Geophysical Union: Washington DC, USA, 2018.
55. Zlotnicki, J.; Sasai, Y.; Johnston, M.J.S.; Fauquet, F.; Villacorte, E.; Cordon, J.M. The 2010 seismovolcanic crisis at Taal Volcano (Philippines). *Earth, Planets Space* **2018**, *70*, 159. [[CrossRef](#)]
56. Maussen, K.; Villacorte, E.; Rebadulla, R.R.; Maximo, R.P.; Debaille, V.; Bornas, M.A.; Bernard, A. Geochemical characterisation of Taal volcano-hydrothermal system and temporal evolution during continued phases of unrest (1991–2017). *J. Volcanol. Geotherm. Res.* **2018**, *352*, 38–54. [[CrossRef](#)]
57. Zlotnicki, J.; Vargemezis, G.; Johnston, M.; Sasai, Y.; Reniva, P.; Alanis, P. Very-low-frequency resistivity, self-potential and ground temperature surveys on Taal volcano (Philippines): Implications for future activity. *J. Volcanol. Geotherm. Res.* **2017**, *340*, 180–197. [[CrossRef](#)]
58. Moxham, R.M. Changes in surface temperature at Taal Volcano, Philippines 1965 – 1966. *Bull. Volcanol.* **1967**, *31*, 215–234. [[CrossRef](#)]
59. Rivera, A.M.; Amelung, F.; Albino, F.; Gregg, P.M. Impact of Crustal Rheology on Temperature-Dependent Viscoelastic Models of Volcano Deformation: Application to Taal Volcano, Philippines. *J. Geophys. Res. Solid Earth* **2019**, *124*, 978–994. [[CrossRef](#)]
60. Hubanks, P.A.; King, M.D.; Platnick, S.; Pincus, R. *MODIS Atmosphere L3 Gridded Product Algorithm Theoretical Basis Document*; ATBD Reference Number: ATBD-MOD-30; NASA GSFC: Greenbelt, MD, USA, 2008.
61. Teixeira, A.S.T.J. *AIRS/Aqua L3 Daily Standard Physical Retrieval (AIRS-only) 1 Degree x 1 degree V006*; Goddard 15 Earth Sciences Data and Information Services Center (GES DISC): Greenbelt, MD, USA, 2013. [[CrossRef](#)]
62. Teixeira, A. *AIRS/Aqua L3 Daily Standard Physical Retrieval (AIRS-only) 1 Degree x 1 Degree V006*; Goddard 15 Earth Sciences Data and Information Services Center (GES DISC): Greenbelt, MD, USA, 2013. [[CrossRef](#)]
63. Krotkov, N.; Li, C.; Leonard, P. *OMI/Aura Sulfur Dioxide (SO₂) Total Column L3 1 Day Best Pixel in 0.25 Degree x 0.25 Degree V3*; Goddard Earth Sciences Data and Information Services Center (GES DISC): Greenbelt, MD, USA, 2015; Volume V3. [[CrossRef](#)]
64. Theys, N.; De Smedt, I.; Yu, H.; Danckaert, T.; Van Gent, J.; Hörmann, C.; Wagner, T.; Hedelt, P.; Bauer, H.; Romahn, F.; et al. Sulfur dioxide retrievals from TROPOMI onboard Sentinel-5 Precursor: Algorithm theoretical basis. *Atmospheric Meas. Tech.* **2017**, *10*, 119–153. [[CrossRef](#)]

65. Spurr, R.; Loyola, D.; Roozendael, M.; Lerot, C. S5P/TROPOMI Total Ozone ATBD. S5P-L2-DLR-ATBD-400A. 2016. Available online: <http://www.tropomi.eu/sites/default/files/files/Sentinel-5P-TROPOMI-ATBD-Total-Ozone.pdf> (accessed on 3 March 2020).
66. Vidot, J.; Landgraf, J.; Hasekamp, O.; Butz, A.; Galli, A.; Tol, P.; Aben, I. Carbon monoxide from shortwave infrared reflectance measurements: A new retrieval approach for clear sky and partially cloudy atmospheres. *Remote Sens. Environ.* **2012**, *120*, 255–266. [[CrossRef](#)]
67. Holben, B.; Eck, T.; Slutsker, I.; Tanre, D.; Buis, J.; Setzer, A.; Vermote, E.; Reagan, J.; Kaufman, Y.; Nakajima, T.; et al. AERONET—A Federated Instrument Network and Data Archive for Aerosol Characterization. *Remote Sens. Environ.* **1998**, *66*, 1–16. [[CrossRef](#)]
68. Dubovik, O.; King, M.D. A flexible inversion algorithm for retrieval of aerosol optical properties from Sun and sky radiance measurements. *J. Geophys. Res.* **2000**, *105*, 20673–20696. [[CrossRef](#)]
69. Dubovik, O.; Smirnov, A.; Holben, B.N.; King, M.; Kaufman, Y.J.; Eck, T.F.; Slutsker, I. Accuracy assessments of aerosol optical properties retrieved from Aerosol Robotic Network (AERONET) Sun and sky radiance measurements. *J. Geophys. Res. Space Phys.* **2000**, *105*, 9791–9806. [[CrossRef](#)]
70. Wong, A.; Keeley, R.; Carval, T. Argo quality control manual for CTD and trajectory data. *Argo10* **2019**. [[CrossRef](#)]
71. D’Asaro, E.A.; McNeil, C. Calibration and Stability of Oxygen Sensors on Autonomous Floats. *J. Atmospheric Ocean. Technol.* **2013**, *30*, 1896–1906. [[CrossRef](#)]
72. Theys, N.; Champion, R.; Clarisse, L.; Brenot, H.; Van Gent, J.; Dils, B.; Corradini, S.; Merucci, L.; Coheur, P.-F.; Van Roozendael, M.; et al. Volcanic SO₂ fluxes derived from satellite data: a survey using OMI, GOME-2, IASI and MODIS. *Atmos. Chem. Phys. Discuss.* **2013**, *13*, 5945–5968. [[CrossRef](#)]
73. Brenna, H.; Kutterolf, S.; Krüger, K. Global ozone depletion and increase of UV radiation caused by pre-industrial tropical volcanic eruptions. *Sci. Rep.* **2019**, *9*, 9435. [[CrossRef](#)]
74. Xu, L.; Wei, K.; Wu, X.; Smyshlyayev, S.P.; Chen, W.; Galin, V.Y. The Effect of Super Volcanic Eruptions on Ozone Depletion in a Chemistry–Climate Model. *Adv. Atmos. Sci.* **2019**, *36*, 823–836. [[CrossRef](#)]
75. Klobas, J.; Wilmouth, D.M.; Weisenstein, D.K.; Anderson, J.G.; Salawitch, R.J. Ozone depletion following future volcanic eruptions. *Geophys. Res. Lett.* **2017**, *44*, 7490–7499. [[CrossRef](#)]
76. Wardell, L.; Kyle, P.; Chaffin, C. Carbon dioxide and carbon monoxide emission rates from an alkaline intra-plate volcano: Mt. Erebus, Antarctica. *J. Volcanol. Geotherm. Res.* **2004**, *131*, 109–121. [[CrossRef](#)]
77. Jimenez-Escalona, J.C.; Raga, G.B.; Baumgardner, D.; Castro, T.; Rosas, I.; Baez, A.; Morton, O. On the Composition of Airborne Particles Influenced by Emissions of the Volcano Popocatepetl in Mexico. *Nat. Hazards* **2004**, *31*, 21–37. [[CrossRef](#)]
78. Robrecht, S.; Vogel, B.; Groß, J.-U.; Rosenlof, K.H.; Thornberry, T.; Rollins, A.; Krämer, M.; Christensen, L.; Müller, R. Mechanism of ozone loss under enhanced water vapour conditions in the mid-latitude lower stratosphere in summer. *Atmos. Chem. Phys. Discuss.* **2019**, *19*, 5805–5833. [[CrossRef](#)]
79. Dey, S.; Singh, R.P. Surface latent heat flux as an earthquake precursor. *Nat. Hazards Earth Syst. Sci.* **2003**, *3*, 749–755. [[CrossRef](#)]
80. Papasimakis, N.; Cervone, G.; Pallikari, F.; Kafatos, M. Multifractal character of surface latent heat flux. *Phys. A: Stat. Mech. Appl.* **2006**, *371*, 703–718. [[CrossRef](#)]
81. Sugimoto, S.; Hanawa, K. Roles of SST Anomalies on the Wintertime Turbulent Heat Fluxes in the Kuroshio–Oyashio Confluence Region: Influences of Warm Eddies Detached from the Kuroshio Extension. *J. Clim.* **2011**, *24*, 6551–6561. [[CrossRef](#)]
82. Lee, C.; Kim, Y.J.; Tanimoto, H.; Bobrowski, N.; Platt, U.; Mori, T.; Yamamoto, K.; Hong, C.S. High ClO and ozone depletion observed in the plume of Sakurajima volcano, Japan. *Geophys. Res. Lett.* **2005**, *32*. [[CrossRef](#)]
83. Gerlach, T. Volcanic sources of tropospheric ozone-depleting trace gases. *Geochem. Geophys. Geosyst.* **2004**, *5*. [[CrossRef](#)]
84. Pittman, J.V.; Pan, L.L.; Wei, J.C.; Irion, F.W.; Liu, X.; Maddy, E.; Barnet, C.D.; Chance, K.; Gao, R.-S. Evaluation of AIRS, IASI, and OMI ozone profile retrievals in the extratropical tropopause region using in situ aircraft measurements. *J. Geophys. Res. Space Phys.* **2009**, *114*. [[CrossRef](#)]

